

Effects of B₂O₃ on Crystallization, Structure, and Heat Transfer of CaO-Al₂O₃-Based Mold Fluxes



JIAN YANG, JIANQIANG ZHANG, OLEG OSTROVSKI, CHEN ZHANG,
and DEXIANG CAI

The reaction between traditional CaO-SiO₂-based mold fluxes and high-Al steel inevitably changes flux composition, and, consequently, flux properties. This problem can be mitigated by using CaO-Al₂O₃-based mold fluxes. To maintain appropriate melting properties, CaO-Al₂O₃-based mold fluxes contain B₂O₃, which is an effective fluxing agent that decreases the liquidus temperature. In this article, the effects of B₂O₃ on crystallization behavior, structure, and heat transfer of CaO-Al₂O₃-based mold fluxes were studied using single/double hot thermocouple technique, Raman spectroscopy, and infrared emitter technique. The increase of B₂O₃ content from 7.6 to 13.1 mass pct suppressed the crystallization tendency of mold fluxes in continuous cooling experiments and isothermal experiments conducted over 1273 K (1000 °C). The isothermal crystallization below 1273 K (1000 °C) was also inhibited when B₂O₃ content increased from 7.6 to 9.6 mass pct; but a further increase of B₂O₃ content to 13.1 mass pct did not show a visible effect on the crystallization tendency. The increase of B₂O₃ content from 9.6 to 13.1 mass pct improved the heat fluxes under an incident thermal radiation of 1.6 MW/m²; however, the increase of B₂O₃ content from 7.6 to 9.6 mass pct slightly decreased the heat transfer rate. Crystallization of fluxes and heat transfer were discussed in relation to flux structure.

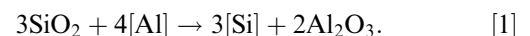
<https://doi.org/10.1007/s11663-018-1467-5>

© The Minerals, Metals & Materials Society and ASM International 2018

I. INTRODUCTION

ADVANCED high-strength steels (AHSSs) feature high mechanical strength, ductility, and low density, showing a great potential in the modern automotive industry. Twinning-induced plasticity (TWIP) austenitic steel, a new generation of AHSS, with extraordinary mechanical properties has high concentrations of Mn and Al.^[1–5] The addition of Mn provides a complex strain-hardening behavior due to its moderate stacking fault energy (20 to 40 mJ/m²) at room temperature.^[1,2] Al reduces the density of TWIP steel, making automobiles lighter. Moreover, the addition of Al stabilizes the formation of deformation twinning and avoids the transformation of austenite to ε-martensite at low strains, which enhanced the elongation of TWIP steel.^[6] However, Al in molten steel inevitably reacts with SiO₂

in the conventional CaO-SiO₂-based mold fluxes at high temperature (Eq. [1]), which causes the decrease of SiO₂ and the accumulation of Al₂O₃ in molten fluxes.^[7–9]



The changing composition makes the in-mold performances of mold fluxes unpredictable in the casting of high-Al steel, considerably increasing the likelihood of sticker breakout and surface imperfections. Therefore, it is indispensable to mitigate the reaction between molten steel and fluxes. CaO-Al₂O₃-based mold fluxes with low concentration of SiO₂ were proposed to depress the driving force for reaction [1]. But the increase of Al₂O₃ and decrease of SiO₂ concentrations raise the liquidus temperature of CaO-Al₂O₃-based mold fluxes compared with that of CaO-SiO₂-based mold fluxes.^[10] In this way, fluxing agents have to be added into CaO-Al₂O₃-based mold fluxes to ensure appropriate viscosity and melting properties.^[11–17] The substitution of BaO for CaO was found to inhibit the crystallization tendency in CaO-Al₂O₃-based fluxes^[15]; Li₂O and Na₂O could lower the initial crystallization temperature, which may benefit the infiltration of the fluxes^[16]; MnO was also found to reduce the melting temperature of CaO-Al₂O₃-based fluxes.^[17] B₂O₃ is a commonly used fluxing agent that effectively ameliorates the melting properties and viscosity of CaO-SiO₂-based mold fluxes.^[11–14] Although

JIAN YANG, JIANQIANG ZHANG, and OLEG OSTROVSKI are with the School of Materials Science and Engineering, University of New South Wales, Sydney, NSW, 2052, Australia. Contact e-mail: j.q.zhang@unsw.edu.au CHEN ZHANG and DEXIANG CAI are with the Baosteel Group Corporation Research Institute, Shanghai 201900, China.

Manuscript submitted July 11, 2018.

Article published online November 30, 2018.

B₂O₃ also reacts with [Al] at high temperature,^[18] its amount can be optimized to achieve reasonable lubricity at a weaker reactivity.

B₂O₃ is a network former in CaO-SiO₂-based mold fluxes, polymerizing the silicate network through changing the silicate structure by reacting with non-bridging oxygen^[14,19–23], or by forming 3-D borate structural groups.^[14,20–22] However, the structure of CaO-Al₂O₃-based system containing B₂O₃ is different. FTIR and Raman spectroscopy analyses of CaO-Al₂O₃-Na₂O-B₂O₃ fluxes by Kim and Sohn^[24] showed that the alumino-borate structures consist of [AlO₄]-tetrahedral, [BO₃]-trigonal, and [BO₄]-tetrahedral structural units. They demonstrated that the increase of B₂O₃ content in CaO-Al₂O₃-based mold fluxes transformed the 3-D complex borate structure to a simpler 2-D borate structure and decreased the percentage of [AlO₄]-tetrahedral units, which decreased the flux viscosity. Xiao *et al.*^[25] showed that the synergic effect of BaO and B₂O₃ improved crystallization tendency of mold fluxes. Blazek *et al.*^[10] indicated that the addition of 15 mass pct B₂O₃ to the fluxes maintained an amorphous structure and decreased the liquidus temperature of mold fluxes in the plant trial. However, the effect of B₂O₃ on crystallization, structure, and heat transfer of CaO-Al₂O₃-based mold fluxes needs a further systematic study. In this work, the crystallization behavior, structure and heat transfer of mold fluxes with different B₂O₃ content were studied using single/double hot thermocouple technique (SHTT/DHTT), Raman spectroscopy, and infrared emitter technique (IET). The aim of this investigation is to pave the way for the application of CaO-Al₂O₃-based mold fluxes in the continuous casting of high-Al TWIP steel.

II. EXPERIMENTAL METHODS

A. Sample Preparation

Pre-mixed reagent grade CaCO₃, SiO₂, Al₂O₃, B₂O₃, Na₂CO₃, MgO, Li₂CO₃, and CaF₂ powders were melted at 1673 K (1400 °C) in graphite crucibles for 20 minutes at which CaCO₃, Na₂CO₃, and Li₂CO₃ decomposed to corresponding oxides. The melted fluxes were quenched in distilled water and then ground into powders using a ring mill. Chemical compositions of the as-quenched samples are listed in Table I, marked as Samples 1 to 4. The concentrations of B₂O₃ and Li₂O were determined by inductively coupled plasma-optical emission spectroscopy analysis (Thermo Scientific IRIS Intrepid II, MA), and other components were analyzed by X-ray

fluorescence (XRF) (PANalytical AXIOS-Advanced WDXRF spectrometer, Netherland). The as-quenched samples exhibited complete amorphous structure as examined using X-ray diffraction (XRD) except Sample 1, in which a very small amount of crystals was identified in otherwise amorphous structure as shown in Figure 1. Hemispheric temperature, T_{hem} , measured using hot stage microscopy, is also listed in Table I to reflect the melting properties of mold fluxes. It was defined as the temperature at which the height of a flux cylinder decreased to 50 pct of its original height during a continuous heating process. The details of this measurement are described elsewhere.^[26]

B. Experimental Apparatus

1. Hot thermocouple technique

The crystallization behavior of mold fluxes was studied using SHTT/DHTT (Professional Engineer Office KONNO, Japan)^[27–29] schematically illustrated in Figure 2(a). Due to the low thermal inertia of the system, SHTT/DHTT enables a high heating/cooling rate up to ± 30 K/s by system control, which makes it capable of simulating the highest cooling rate that mold fluxes encounter in the infiltration process.^[28,30] Mold fluxes (ca. 10 mg) were mounted on a B-type thermocouple tip, and then heated or cooled in accordance with the programmed temperature profile in SHTT experiments, while the sample was attached between two thermocouples in DHTT experiments, as shown in Figure 2(b). The crystallization process of mold fluxes was *in situ* observed and recorded by a video camera.

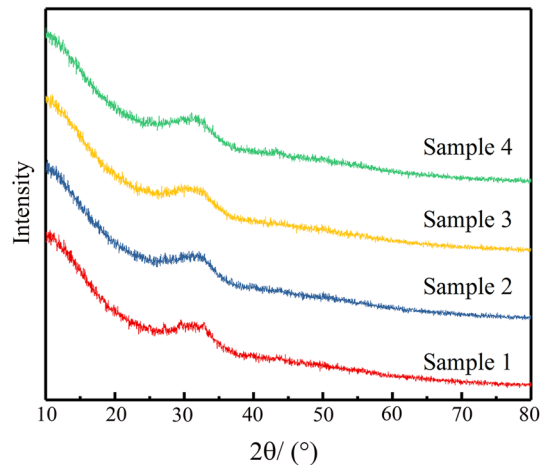


Fig. 1—XRD patterns of as-quenched mold fluxes.

Table I. Chemical Composition of CaO-Al₂O₃-Based Mold Fluxes (Mass Pct)

Samples	CaO	Al ₂ O ₃	SiO ₂	B ₂ O ₃	Na ₂ O	MgO	Li ₂ O	<i>F</i>	T_{hem} [K (°C)]
1	48.9	24.1	6.9	7.6	5.6	1.4	2.1	3.4	1437 (1164)
2	47.6	23.1	7.0	9.6	5.9	1.5	2.1	3.2	1366 (1093)
3	45.9	22.8	6.9	11.7	5.5	1.7	2.1	3.4	1340 (1067)
4	44.6	22.0	7.0	13.1	6.1	1.6	2.2	3.4	1305 (1032)

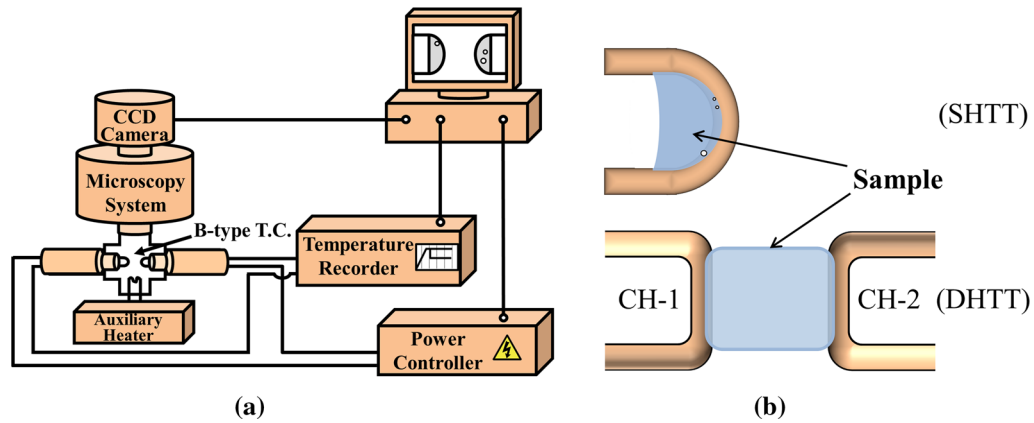


Fig. 2—Schematics of (a) hot thermocouple technique and (b) thermocouple setup in SHTT/DHTT.

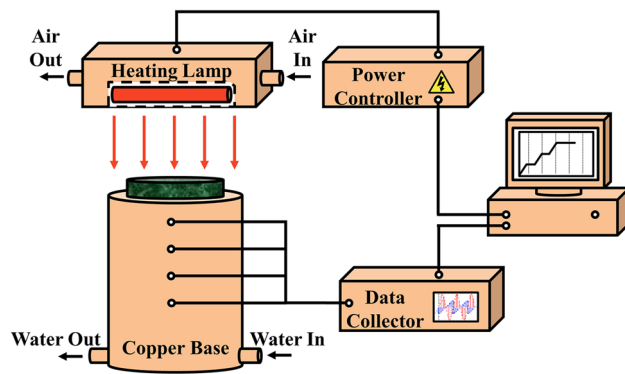


Fig. 3—Schematics of IET system.

2. Infrared emitter technique

IET (Central South University, China) was employed to study the heat transfer rate across mold fluxes. The schematics of IET is illustrated in Figure 3. The thermal radiation with programmed intensity is released from a heating lamp with a set of tungsten filaments to a mold flux disk of a standard size. Four thermocouples are embedded in the copper base underneath the flux disk to measure the temperature gradient. The heat flux across the mold flux disk is calculated according to Fourier's law^[31]:

$$q = \frac{-1}{n} \sum_i k \left(\frac{dT}{dx} \right)_i, \quad [2]$$

where q is the heat flux, n is the number of thermocouple pairs, k is the thermal conductivity of copper.

C. Experimental Procedures

1. Crystallization behavior measurement

The *in situ* crystallization behavior of mold fluxes in continuous cooling and isothermal experiments was studied using SHTT. The sample mounted on the thermocouple tip was heated to 1773 K (1500 °C) with a heating rate of 30 K/s and held at 1773 K (1500 °C) for 1 minutes for homogenization and bubble removal.

Afterward, two cooling strategies were applied to the mold fluxes, as illustrated in Figures 4(a) and (b). In the continuous cooling experiments, the sample was cooled down to 1073 K (800 °C) with different cooling rates. The time and temperature at which the crystallinity of mold fluxes reached 0.5 vol. pct were used to construct continuous cooling transformation (CCT) diagrams. Three replicate tests were conducted for the determination of crystallization temperatures at each cooling rate. In isothermal experiments, the sample was rapidly cooled down to the target temperatures with a cooling rate of 30 K/s and held at those temperatures until the crystallinity reached 100 pct. The times, at which crystallinity reached 0.5 and 99 vol. pct, were used to construct time–temperature transformation (TTT) diagrams, representing the onset and end of crystallization, respectively. Similarly, three replicate measurements were conducted for the determination of crystallization times at different temperatures.

To identify the melting property of Sample 1, in which a tiny amount of crystals was found in the as-quenched samples, the melting temperature range of this sample was also observed during the heating process in continuous cooling and isothermal experiments.^[17,32]

The crystallization process of mold fluxes in a temperature gradient simulating the thermal field between the solidifying steel and the cold surface of mold flux film in the continuous casting was studied using DHTT. The temperature profile of DHTT experiments is given in Figure 4(c). The sample mounted on the thermocouple tip was heated to 1773 K (1500 °C) with a heating rate of 30 K/s. Then, two thermocouples were intersected and separated to form a flux film of 1.5 mm in between. After holding for 1 minute, one thermocouple was cooled to 873 K (600 °C) to simulate the temperature of the cold side of flux film in continuous casting process^[21,33], while the other thermocouple remained at 1773 K (1500 °C) to simulate the temperature of solidifying steel close to the meniscus zone.^[34] The crystallization behavior of the flux film in such a temperature gradient was recorded for 10 minutes.

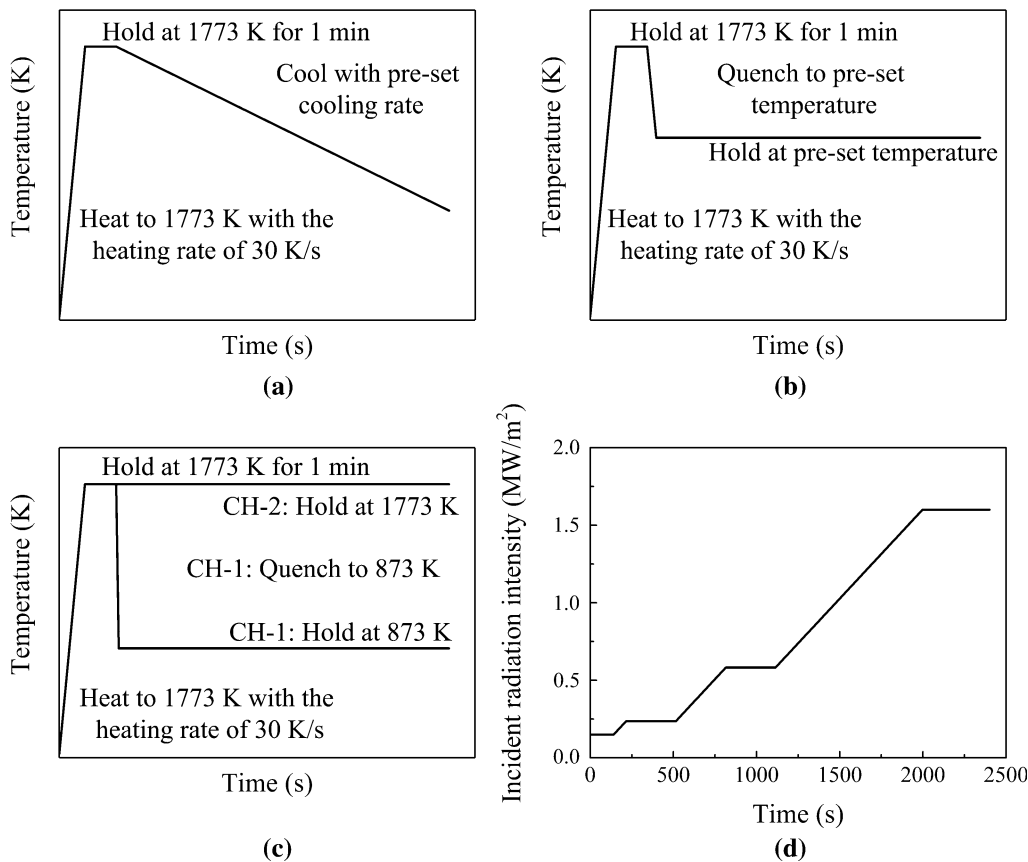


Fig. 4—Schematic temperature profiles in (a) continuous cooling experiments; (b) isothermal experiments; and (c) DHTT experiments; power profile in (d) IET experiments.

2. Precipitated phases analysis

XRD (PANalytical X'pert Multipurpose X-ray Diffraction System, Netherlands) with Cu K α radiation was used to determine the crystalline phases formed in Samples 1 to 4 at different temperatures. The as-quenched mold fluxes were heat-treated at 1173 K (900 °C), 1273 K (1000 °C), and 1373 K (1100 °C) in a muffle furnace for 20 minutes. Then, the sample was quenched into distilled water. The precipitated phases of the milled samples were scanned using XRD within the scanning range of $2\theta = 10$ to 80 deg. The XRD patterns were analyzed using HighScore Plus 4.0.

3. Structure analysis

Raman spectroscopy (Renishaw inVia Raman Microscope, UK) was employed to study the structural change of mold fluxes with different B₂O₃ contents. The as-quenched mold fluxes were ground and gently pressed into a pellet with a thickness of 2 mm. It was illuminated with an Ar-ion laser beam at room temperature. The excitation wavelength of Ar-ion laser was 514 nm with a beam spot size of 1.5 μ m. In the measurement, the Raman shift ranged from 450 to

1700 cm^{-1} , and the Raman spectra bands were deconvoluted based on Gaussian distribution using WiRE 3.4 software.

4. Heat flux measurement

The heat flux across the flux disk was examined using IET. The fabrication of the flux disk followed the procedure: (1) approximately 13 g mold fluxes were melted at 1673 K (1400 °C) for 20 minutes in a muffle furnace; (2) the molten mold fluxes were poured into a cylinder copper mold with an inner diameter of 40 mm and pressed to a disk; (3) the pressed mold flux disk was immediately placed in another muffle furnace in which the temperature gradually decreased from 1073 K (800 °C) to 298 K (25 °C) with a slow cooling rate of 1 K/min to minimize the internal stress within the disk; (4) the heat-treated mold flux disk was ground to a thickness of 4 mm, and then polished using sandpapers from 300 to 1200 grits. In the heat flux measurement, the prepared mold flux disk ($\Phi 40 \times 4$ mm) was placed on the copper base of the IET system. The radiation was emitted in accordance with a stepwise power profile presented in Figure 4(d). The incident thermal radiation

was increased to 1.6 MW/m^2 , which is close to the radiation released from the steel strand in continuous casting. The temperatures recorded by the embedded thermocouples were used for the heat flux calculation.

III. RESULTS

A. Continuous Cooling Experiments

CCT diagrams of Samples 1 to 4 are presented in Figures 5(a) through (d) and compared in Figure 5(e). The critical cooling rate, above which crystallization did not occur during continuous cooling process, decreased from 10 to 5 K/s when B_2O_3 content increased from 7.6 to 9.6 mass pct. A further increase of B_2O_3 content to 11.8 and 13.1 mass pct did not reduce the critical cooling rate but decreased the crystallization temperature at a given cooling rate. For example, at a fixed cooling rate of 5 K/s, the average crystallization temperature decreased from 1322 K (1049 °C) to 1264 K (991 °C), 1180 K (907 °C), and 1159 K (886 °C) when B_2O_3 content increased from 7.6 to 9.6, 11.8, and 13.1 mass pct.

The melting temperature range of Sample 1 during heating process is illustrated in Figure 6. Sample 1 started to melt at 1413 K (1140 °C); the melting process ended at 1535 K (1262 °C), after which bubbles were formed. Sample 1 was visually completely melted at 1673 K (1400 °C). However, it is noted that the liquid flux pool of Sample 1 was not as transparent as other samples at high temperature, *e.g.*, Sample 2 as given in Figure 6. It indicates that there might be some unobservable solid particles existing in Sample 1 at high temperature, which is in line with the observation of tiny

peaks in the XRD pattern of Sample 1. But they did not result in a strong crystallization tendency, or notably increase the crystallization temperature of Sample 1.

B. Isothermal Experiments

TTT diagrams of Samples 1 to 4 are presented in Figures 7(a) through (d). A comparison of the onsets of crystallization in TTT diagrams of different samples is shown in Figure 7(e). The shortest incubation time in the crystallization of Sample 1 was 7 seconds. The increase of B_2O_3 content from 7.6 to 9.6 mass pct increased the shortest incubation time to 11 seconds. A further increase of B_2O_3 content had no significant

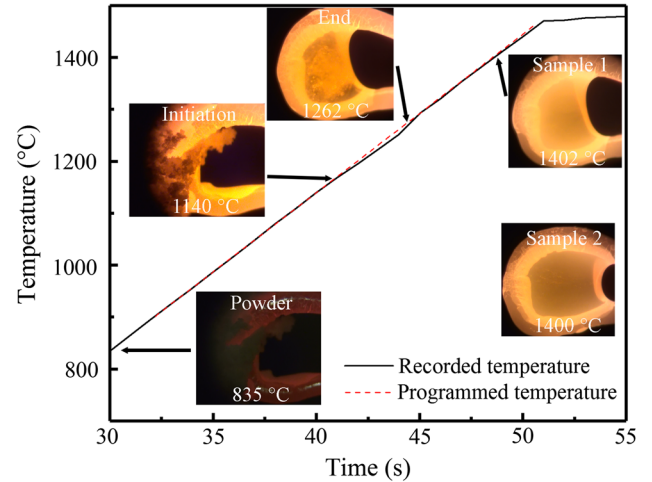


Fig. 6—Melting temperature range observation of Sample 1.

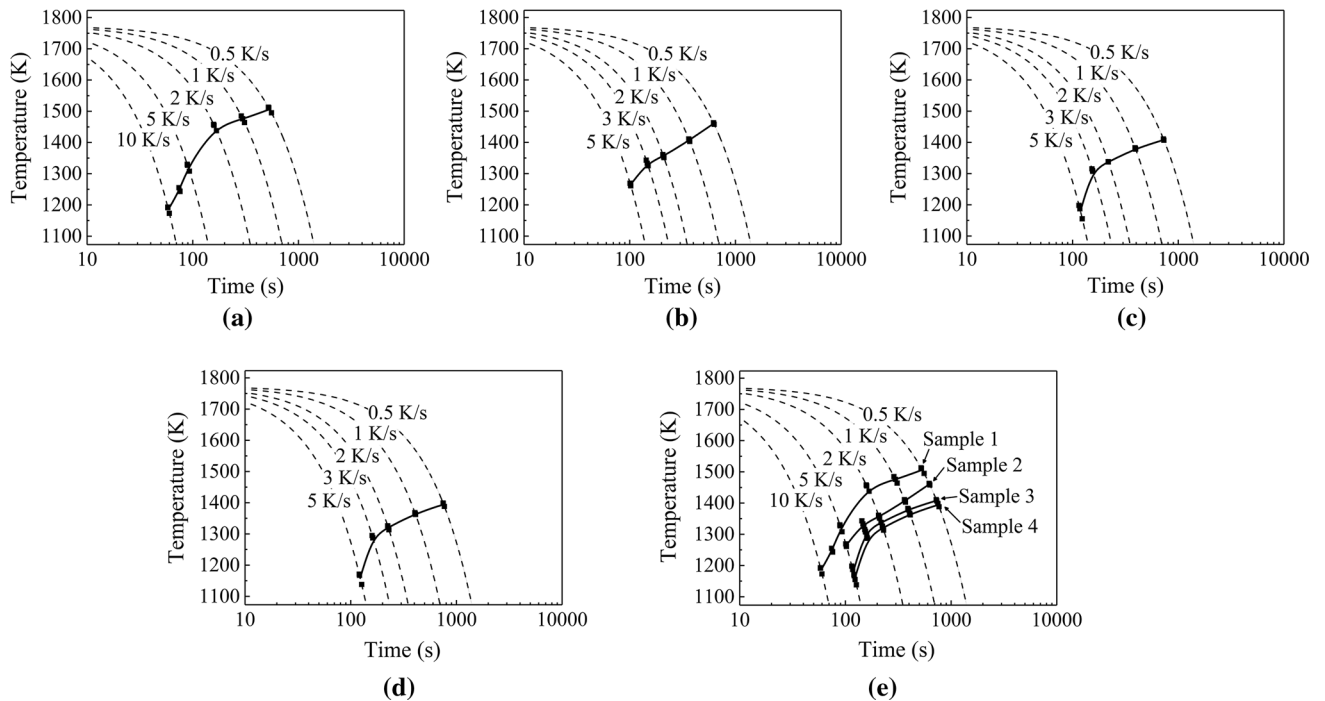


Fig. 5—CCT diagrams of mold fluxes: (a) to (d) Samples 1 to 4; (e) comparison of CCT diagrams of Samples 1 to 4.

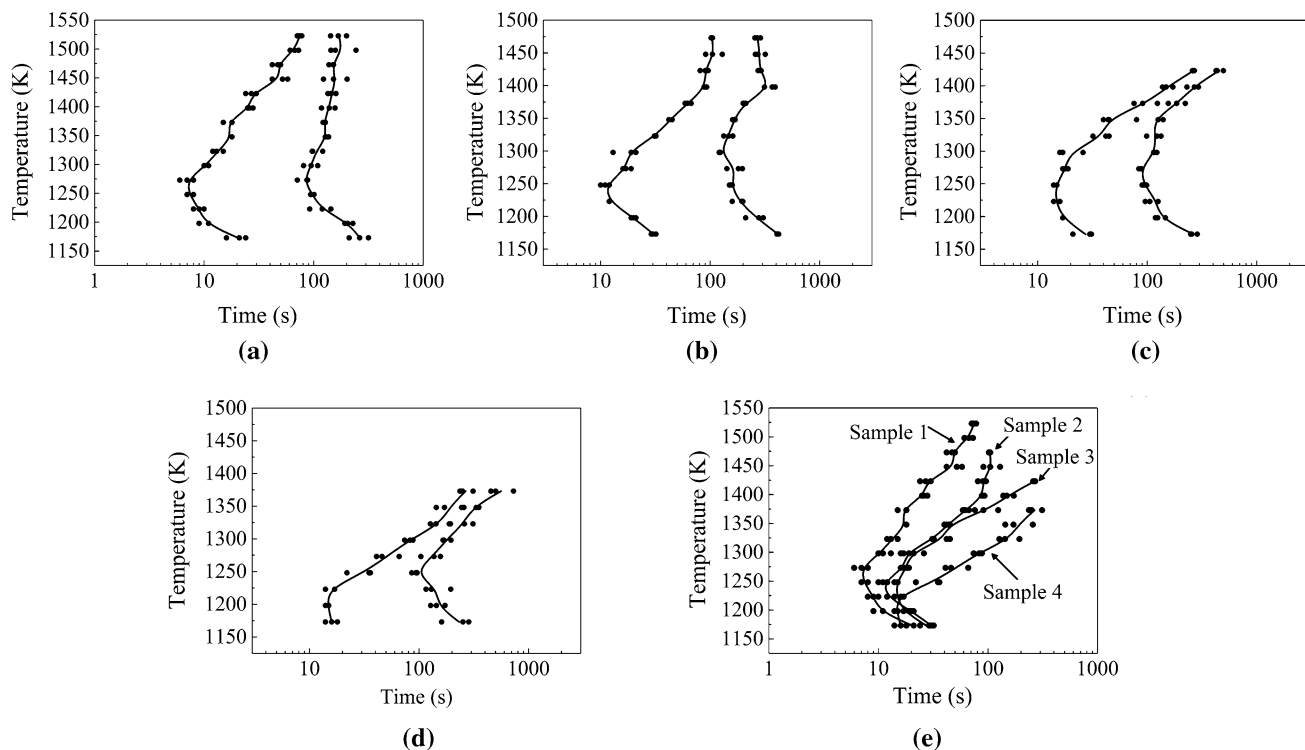


Fig. 7—TTT diagrams of mold fluxes: (a) to (d) Samples 1 to 4; (e) comparison of TTT diagrams for the onsets of crystallization of Samples 1 to 4.

effect on the incubation time in the crystallization of Samples 2 to 4 below 1273 K (1000 °C). However, it is noticeable that the incubation times of mold fluxes over 1273 K (1000 °C) were extended with the increase of B_2O_3 content from 7.6 to 13.1 mass pct.

The precipitated phases of mold fluxes with different B_2O_3 contents at 1173 K (900 °C), 1273 K (1000 °C), and 1373 K (1100 °C) examined using XRD analysis are shown in Figure 8. Figure 8(a) presents the XRD pattern of Sample 1 (7.6 mass pct B_2O_3). Four major phases with similar primary peak intensities were found at 1173 K (900 °C) including $Ca_5Al_6O_{14}$, $Ca_5(BO_3)_3F$, $Ca_{14}Mg_2(SiO_4)_8$, and $Ca_3Al_2Si_3O_{12}$. Minor precipitates were also identified, such as $LiAlO_2$ and CaF_2 . In some cases where two peaks of different phases were too close to be separated, the symbol on the top indicates the phase that contributed more in the peak intensity according to the reference patterns. As the temperature increased to 1273 K (1000 °C) and 1373 K (1100 °C), $Ca_5Al_6O_{14}$ dominated the precipitated phases, while the amounts of $Ca_{14}Mg_2(SiO_4)_8$ and $Ca_3Al_2Si_3O_{12}$ decreased. $Ca_5(BO_3)_3F$ disappeared, and $Ca_3B_2O_6$ was formed at 1273 K (1000 °C) whose amount also decreased when temperature increased from 1273 K (1000 °C) to 1373 K (1100 °C). No CaF_2 was detected at high temperature.

The precipitated phases in Sample 2 (9.6 mass pct B_2O_3) are presented in Figure 8(b). $Ca_5(BO_3)_3F$, $Ca_{14}Mg_2(SiO_4)_8$, and $Ca_3Al_2Si_3O_{12}$ were still the major

precipitates at 1173 K (900 °C), while $Ca_5Al_6O_{14}$ showed a lower proportion compared with Sample 1 at this temperature. A small amount of $Ca_3B_2O_6$ was found in Sample 2 at 1173 K (900 °C). Similar to Sample 1, the increase of temperature stimulated the formation of $Ca_5Al_6O_{14}$ which became the major phase at 1373 K (1100 °C) but depressed the precipitation of $Ca_{14}Mg_2(SiO_4)_8$ and $Ca_3Al_2Si_3O_{12}$. The major phase at 1273 K (1000 °C) was $Ca_3B_2O_6$ but no $Ca_5(BO_3)_3F$ was detected. The intensity of $Ca_3B_2O_6$ decreased with the increasing temperature to 1373 K (1100 °C).

The XRD pattern of Sample 3 (11.8 mass pct B_2O_3) is presented in Figure 8(c). The major phases were $Ca_2Al_2SiO_7$ and $Ca_5(BO_3)_3F$ at 1173 K (900 °C). With the increase of temperature, the amount of $Ca_2Al_2SiO_7$ diminished but the proportion of $Ca_5Al_6O_{14}$ increased to a dominant phase at 1373 K (1100 °C). When temperature increased from 1173 K (900 °C) to 1273 K (1000 °C), $Ca_5(BO_3)_3F$ vanished but $Ca_3B_2O_6$ appeared. The intensity of $Ca_3B_2O_6$ peaks largely decreased with a further increase of temperature to 1373 K (1100 °C).

The XRD pattern of Sample 4 (13.1 mass pct B_2O_3) is presented in Figure 8(d). The major phases at 1173 K (900 °C) were $Ca_2Al_2SiO_7$ and $Ca_3B_2O_6$. The intensity of peaks decreased at 1273 K (1000 °C), and no crystalline but amorphous phase was observed in Sample 4 at 1373 K (1100 °C) as shown in the XRD pattern inserted in Figure 8(d).

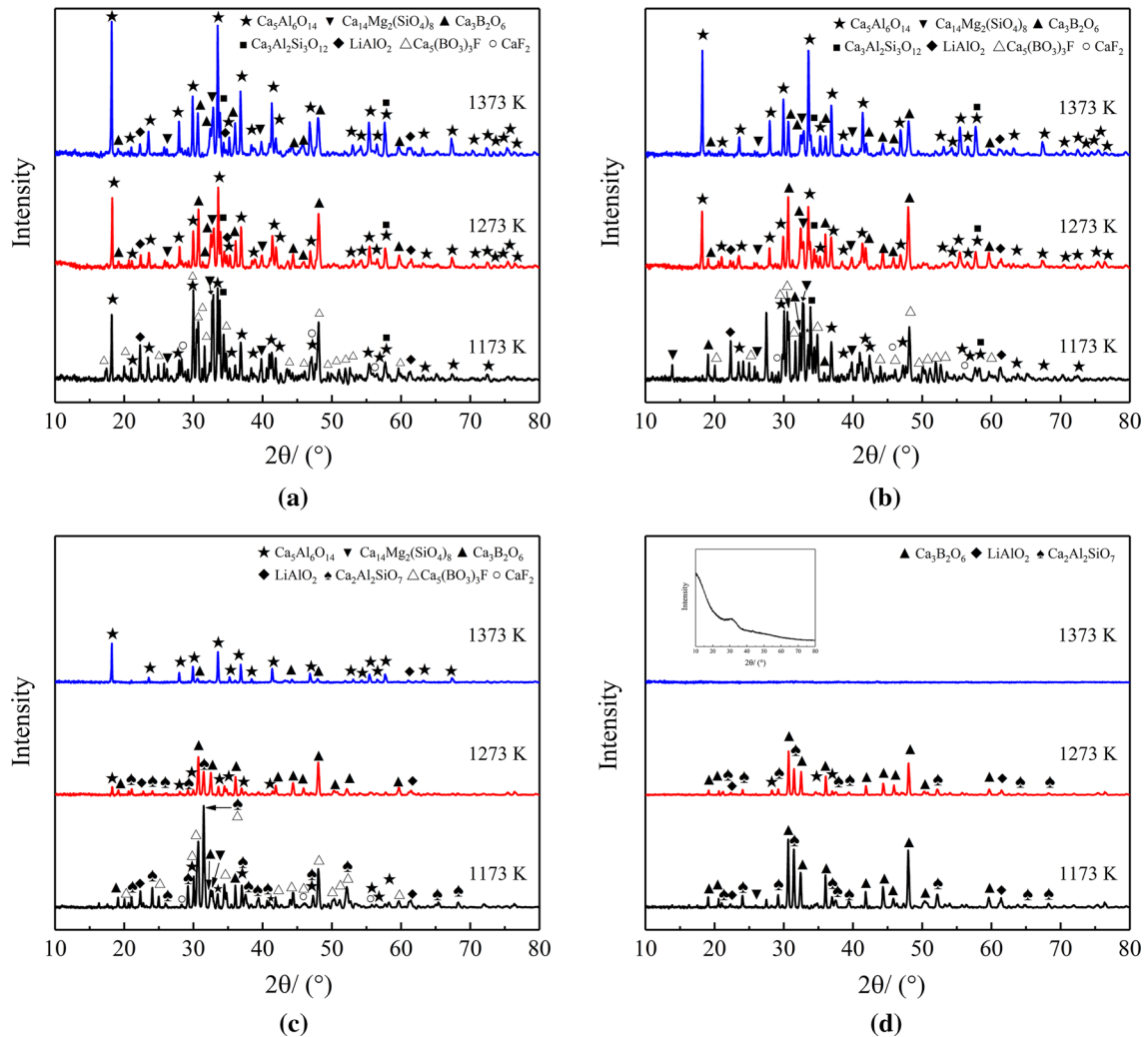


Fig. 8—XRD patterns of mold fluxes quenched at 1173 K (900 °C), 1273 K (1000 °C), and 1373 K (1100 °C): (a) Sample 1; (b) Sample 2; (c) Sample 3; and (d) Sample 4.

C. Double Hot Thermocouple Technique Experiments

The crystallization process of mold fluxes with different B_2O_3 contents in the thermal field set in the DHTT experiments is shown in Figure 9. Figures 9(a1) through (a4) illustrate the crystalline evolution in Sample 1 after the cold side reached 873 K (600 °C). A solid crystalline layer was formed within 60 seconds. The ratio of crystalline layer increased from 37 to 52 pct when crystallization proceeded from 60 to 120 seconds. The crystalline layer further stretched to both high temperature and low temperature ends, achieving the crystallinity of 72 and 84 pct at 300 and 600 seconds, respectively.

Figures 9(b1) through (b4) illustrate the crystal formation process of Sample 2 in the same condition. Only a few nuclei could be traced at 60 seconds. They slowly developed from a small piece of crystals to a solid crystalline layer with a ratio of 52 pct from 120 to 300 seconds. Afterward, the thickness of a crystalline layer increased to 83 pct which was close to that of Sample 1 at 600 seconds.

Figures 9(c1) through (c4) show the crystallization of Sample 3. Similar to Sample 2, a solid crystalline layer in Sample 3 did not grow within the first 120 seconds. Two solid crystalline films were observed at 300 seconds. The thicker one was located at the high temperature side, while the narrower film was formed at low temperature was slightly translucent. Two layers joined to form a thick crystalline layer with an estimated crystallinity of 79 pct at 600 seconds.

Figures 9(d1) through (d4) show the crystallization process of Sample 4 in DHTT experiments. No traceable crystals were formed before 120 seconds. At 300 seconds, some large crystals started to precipitate at the high temperature side, while a thin translucent layer was also formed at low temperature. Afterward, the crystalline layer developed rapidly from 300 to 600 seconds when the crystallinity grew from 13 to 68 pct.

A separate DHTT experiment with Sample 4 was conducted to examine the translucent layer initially formed near the low temperature end at 300 seconds by quenching the flux film to room temperature. The

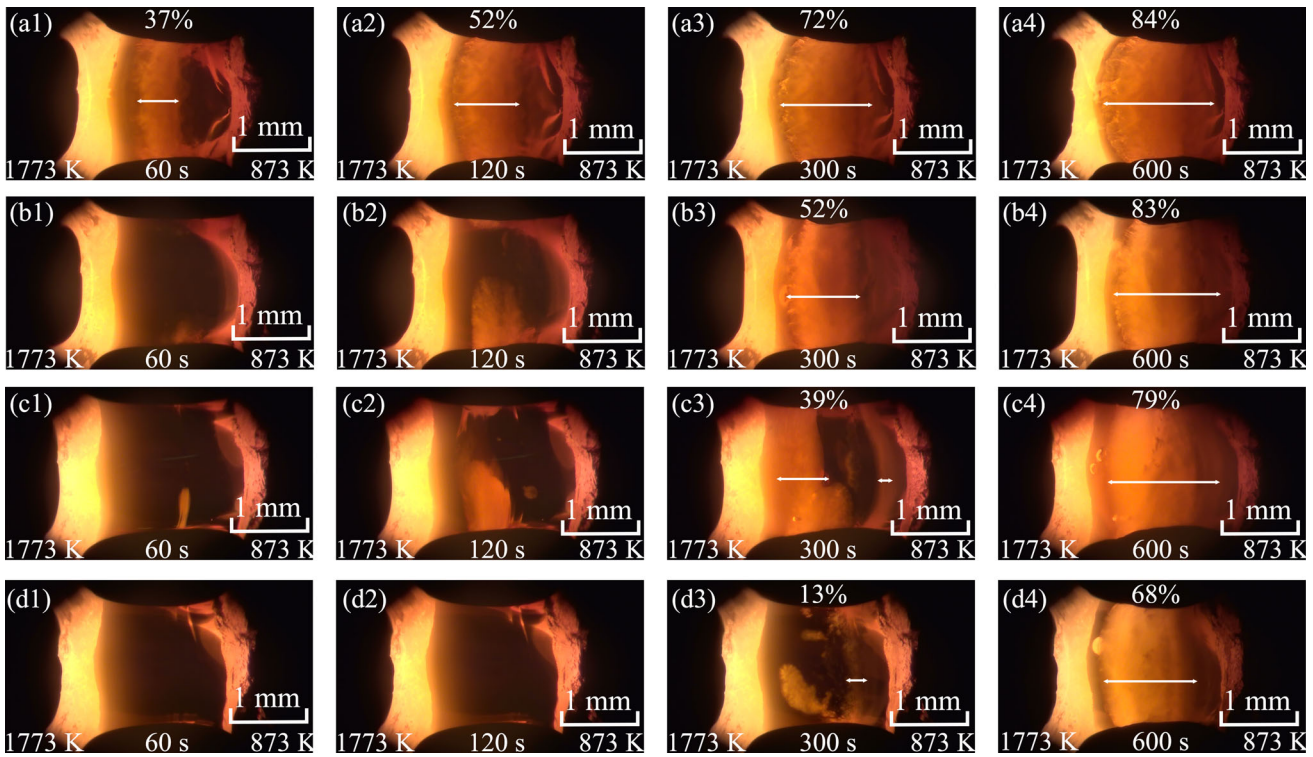


Fig. 9—Crystallization process in DHTT experiments: (a1) through (a4) Sample 1; (b1) through (b4) Sample 2; (c1) through (c4) Sample 3; and (d1) through (d4) Sample 4.

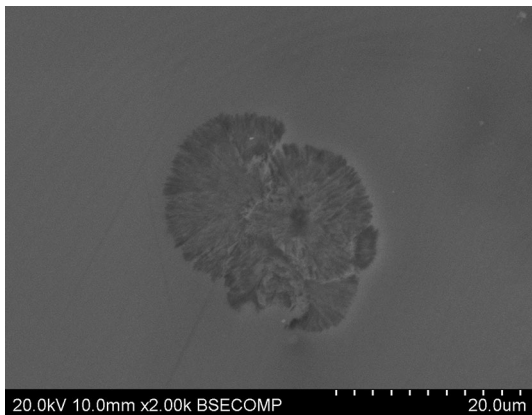


Fig. 10—Morphology of a crystal formed in the translucent layer in DHTT experiments with Sample 4.

scanning electron microscope (SEM) image indicated that the translucent layer was composed of very fine equiaxed crystals with a diameter of less than $20\ \mu\text{m}$ in amorphous matrix as illustrated in Figure 10.

The microstructure of the flux films after DHTT experiments was examined using SEM as shown in Figure 11. The glassy phase on the left side of the flux film was the liquid phase adjacent to the high temperature thermocouple at 1773 K (1500 °C), while the glassy phase on the right side was the original glassy layer attached to the low temperature thermocouple at 873 K (600 °C). Samples 1 and 2 showed more serrated

liquid/crystalline interfaces where dendritic crystals grew, while Samples 3 and 4 exhibited a relatively smooth interface with slim columnar crystals growing toward the heat transfer direction. The middle parts of Samples 1 and 2 exhibited a mesh structure due to a relatively long-time sintering, while Samples 3 and 4 showed a number of irregular bulk crystals in this area. The crystal/glass interfaces were all smooth and perpendicular to the heat transfer direction.

D. Raman Spectroscopy

The deconvoluted Raman spectra of as-quenched samples in the Raman shift range from 450 to $1650\ \text{cm}^{-1}$ are given in Figure 12. The assignments of the peaks in the Raman envelopes are listed in Table II with relevant references. It is noted that Sample 1 contained a tiny amount of crystals, which may not completely indicate the amorphous structure. But the Raman peaks of this sample were generally broad, which is the characteristics of amorphous structure. Therefore, the Raman spectrum of Sample 1 can still be used to be compared with other samples. The bands in 540 to 547 and 591 to $606\ \text{cm}^{-1}$ were assigned to symmetric Al-O⁰ stretching vibration in $[\text{AlO}_4]$ -tetrahedral units^[24,35–38] and $[\text{AlO}_6]$ -octahedral units,^[39–41] respectively. The bands near $760\ \text{cm}^{-1}$ were related to symmetric Al-O⁰ stretching vibration in AlO_2 groups where isolated six-membered rings of $[\text{AlO}_4]^{5-}$ tetrahedron were formed by corner-sharing of two oxygens per tetrahedron^[35–37]; silicate structures (Q^0 , Q^1 and Q^2) were found from 840 to $960\ \text{cm}^{-1}$.^[21,36–38] The bands

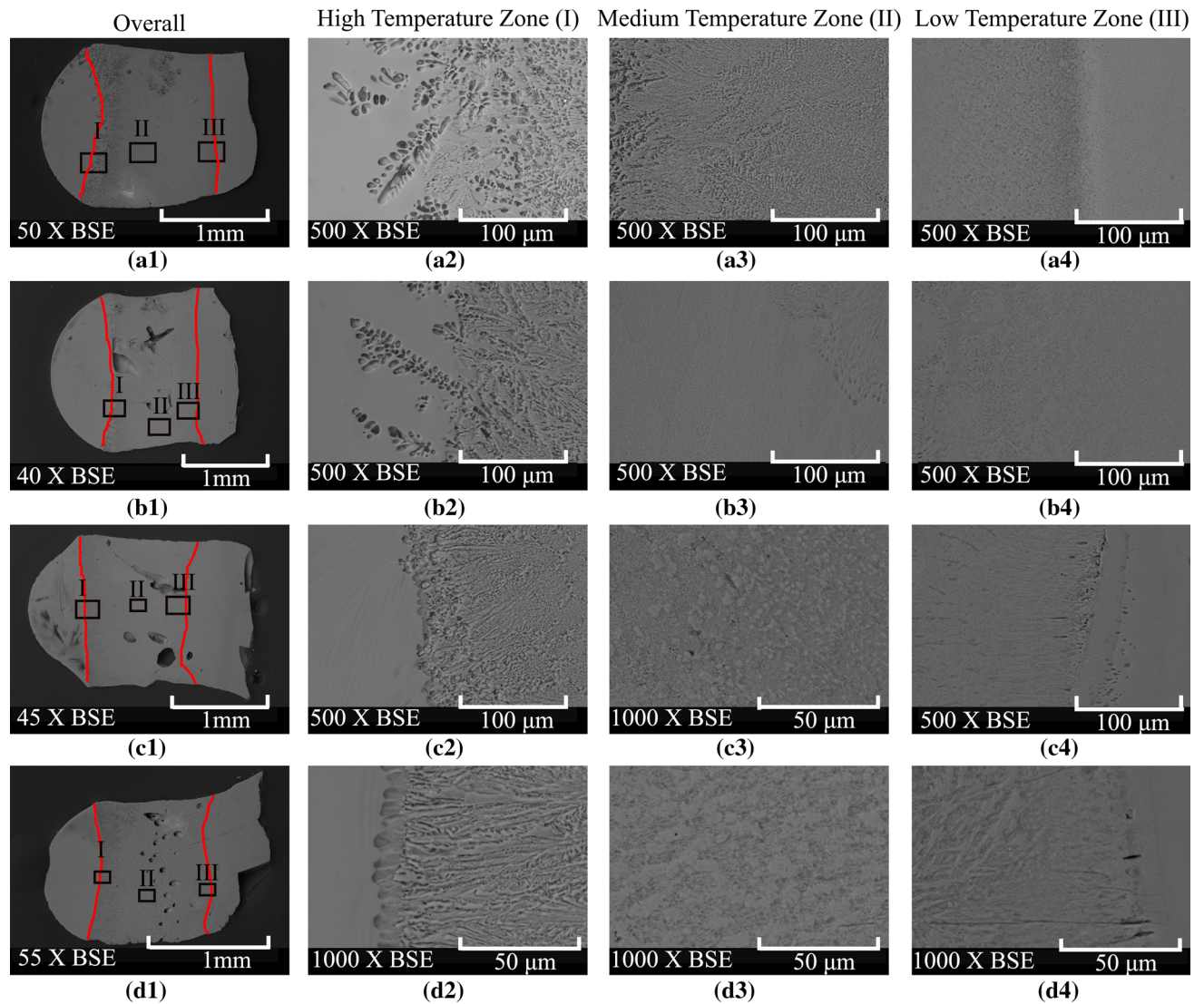


Fig. 11—Microstructure of flux films after DHTT experiments examined using SEM: (a1) through (a4) Sample 1; (b1) through (b4) Sample 2; (c1) through (c4) Sample 3; and (d1) through (d4) Sample 4.

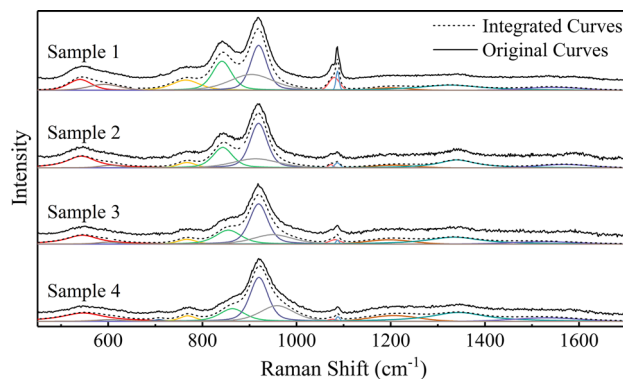


Fig. 12—Deconvoluted Raman spectra of Samples 1 to 4.

near 920 cm^{-1} were assigned to symmetric B-O⁰ stretching vibration in $[\text{BO}_4]$ -pentaborates.^[24,42] The peaks near 1200 cm^{-1} were related to $\text{Al}_{\text{IV}}\text{-O-B}_{\text{IV}}$ bending

vibration^[24] or B-O stretching vibration in $[\text{BO}_4]$ -tetrahedral units.^[21,23] B-O stretching vibration in $[\text{BO}_3]$ -trigonal units attached to various borate groups were identified at 1326 to 1343 and 1524 to 1569 cm^{-1} .^[21–24,42] Two peaks around 1080 cm^{-1} were not assigned to any structures.

Based on the peak areas, $[\text{BO}_4]$ -pentaborate was the major structure in all the samples as shown in Figure 13. The percentages of other borate-related structures, *e.g.*, $\text{Al}_{\text{IV}}\text{-O-B}_{\text{IV}}$, $[\text{BO}_3]$ -trigonal and $[\text{BO}_4]$ -tetrahedral units, increased with the increasing amount of B_2O_3 . The fraction of $[\text{SiO}_4]^{4-}$ (Q^0) decreased when B_2O_3 content increased from 7.6 to 13.1 mass pct. $[\text{Si}_2\text{O}_7]^{6-}$ (Q^1) formed in Samples 1 and 2, while the formation of $[\text{SiO}_3]^{2-}$ (Q^2) was favored in Samples 3 and 4. The aluminate structure was mainly based on $[\text{AlO}_4]$ -tetrahedral units, whose concentration did not visibly change with the variation of B_2O_3 content.

Table II. Assignments of the Peaks in Raman Envelops

Raman Shifts (cm ⁻¹)	B ₂ O ₃ Concentrations (Mass Pct)			Assignments	References
	7.6	9.6	13.1		
540.19	543.23	545.47	546.99	symmetric Al-O ⁰ stretching vibration in [AlO ₄] ⁵⁻	24,35 through 38
591.80	603.94	600.48	605.74	Al-O stretching vibration in [AlO ₆] ⁹⁻	39 through 41
764.71	767.26	767.12	769.11	symmetric Al-O ⁰ stretching vibration in AlO ₂ groups	35 through 37
841.60	843.31	855.23	863.74	Si-O ⁻ stretching vibration in [SiO ₄] ⁴⁻ (Q ⁰)	21,36 through 38
904.44	913.01	—	—	Si-O ⁻ stretching vibration in [Si ₂ O ₇] ⁶⁻ (Q ¹)	21,36 through 38
—	—	949.84	958.69	Si-O ⁻ stretching vibration in [SiO ₃] ³⁻ (Q ²)	21,36 through 38
919.40	919.29	919.44	920.13	symmetric B-O ⁰ stretching vibration in [BO ₄] pentaborate	24,42
1080.05	1072.85	1081.61	1076.45	—	—
1087.06	1086.79	1086.87	1088.01	—	—
1199.77	1207.42	1197.40	1207.12	Al _{IV} -O-B _{IV} bending vibration/B-O stretching vibration in [BO ₄] tetrahedral units	21,23,24
1326.35	1340.99	1335.33	1343.91	B-O stretching vibration in [BO ₃]-trigonal units attached to [BO ₄] units	21 through 24,42
1545.39	1568.89	1524.31	1531.72	B-O stretching vibration in [BO ₃]-trigonal units attached to other [BO ₃] units	21 through 24,42

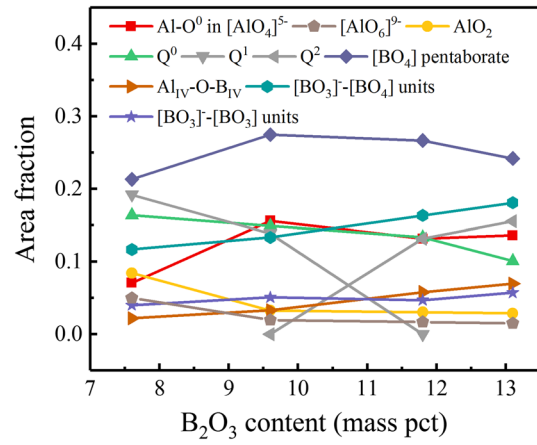


Fig. 13—Area fraction of Raman peaks of mold fluxes with different B₂O₃ contents.

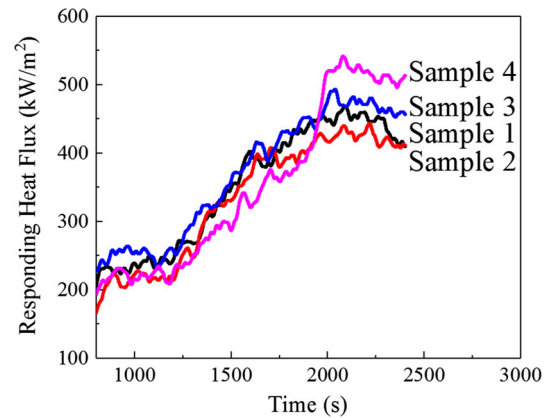


Fig. 14—Heat fluxes of Samples 1 to 4 measured using IET.

E. Heat Transfer Experiments

The heat fluxes of Samples 1 to 4 measured using IET are given in Figure 14. Comparing the heat fluxes when the incident radiation intensity was kept at 1.6 MW/m², the increase of B₂O₃ content from 7.6 to 9.6 mass pct slightly decreased the heat flux from 444 ± 23.4 to 423 ± 17.2 kW/m². A further increase of B₂O₃ content from 9.6 to 11.8 and 13.1 mass pct increased the heat flux from 423 ± 17.2 to 471 ± 19.6 and 517 ± 19.0 kW/m², respectively.

IV. DISCUSSION

A. Crystallization of CaO-Al₂O₃-Based Mold Fluxes

Crystallization of mold fluxes is affected by flux structure and precipitated phases in the fluxes. Continuous cooling and isothermal experiments indicated that the increase of B₂O₃ content inhibited the crystallization process of mold fluxes as shown in Figures 5 and 7, which was consistent with the effect of B₂O₃ on the crystallization of CaO-SiO₂-based mold fluxes.^[21] However, it is noted that the influence of B₂O₃ on crystallization became less significant when B₂O₃ content was

higher than 9.6 mass pct, compared with the effect of B_2O_3 when it was lower than 9.6 mass pct. The critical cooling rates in the continuous cooling experiments and the incubation times in the isothermal crystallization of Samples 2 to 4 were similar in CCT diagrams and the low temperature region in TTT diagrams.

Nucleation and crystal growth rates are related to the high temperature structure of mold fluxes. As follows from Figures 12 and 13, the fraction of $[BO_4]$ -related 3-D structural units visibly increased when B_2O_3 content increased from 7.6 to 9.6 mass pct. The $[BO_4]$ units are normally attached to other borate structures and $[AlO_4]$ -tetrahedral units, considerably increasing the complexity of the network. The percentage of $[AlO_4]$ -tetrahedral units also showed a significant surge when B_2O_3 content increased from 7.6 to 9.6 mass pct, while the Raman band of the more isolated $[AlO_6]^{9-}$ units became less pronounced. The formation of $[SiO_3]^{2-}$ (Q^2) with the decrease of $[SiO_4]^{4-}$ (Q^0) and $[Si_2O_7]^{6-}$ (Q^1) units also raised the degree of polymerization.^[43,44] As an increased structural complexity impeded ionic diffusion in the crystallization process, the increase of B_2O_3 content from 7.6 to 9.6 mass pct resulted in a lower crystallization rate. The further increase of B_2O_3 content from 9.6 to 13.1 mass pct did not increase the degree of polymerization based on fractions of major 3-D borate and aluminate structures, e.g., $[BO_4]$ -pentaborate and $[AlO_4]$ -tetrahedral units. Even a very slight decrease of the fraction of these major 3-D structures was identified in the samples with higher concentration of B_2O_3 while some minor 3-D borate structures took slightly higher portions with the increase of B_2O_3 content, e.g., $[AlO_4]$ - $[BO_4]$ and $[BO_4]$ - $[BO_3]$ structures. The overall amount of $[BO_4]$ -tetrahedral units was in a dynamically stable stage when B_2O_3 content increased from 9.6 to 13.1 mass pct. Although the fraction of $[BO_4]$ -pentaborate slightly decreased, more interactions between $[BO_4]$ units and other structural units, e.g., $[BO_3]$ - and $[AlO_4]$ -units, were traced. Likewise, the overall amount of $[AlO_4]$ -tetrahedral and $[AlO_6]$ -octahedral units were also under a dynamic balance. In this way, the critical cooling rate and the incubation time in the low temperature region did not show visible change when B_2O_3 content increased from 9.6 to 13.1 mass pct.

Crystallization behavior is also related to the precipitated phases of mold fluxes. At 1373 K (1100 °C), the major phase was $Ca_5Al_6O_{14}$ in Sample 1 as shown in Figure 8. The increase of B_2O_3 concentration inhibited not only the precipitation of $Ca_5Al_6O_{14}$, but also the formation of other phases at high temperature. Comparing the incubation times of Samples 1 to 4 at high temperatures in the TTT diagrams (Figure 7) and major phase in XRD patterns at 1273 K (1000 °C) and 1373 K (1100 °C) (Figure 8), it can be suggested that $Ca_5Al_6O_{14}$ exhibited a relatively high formation rate. At 1173 K (900 °C), the XRD analysis indicates that the increase of B_2O_3 content gradually inhibited the formation of $Ca_5Al_6O_{14}$, which was the major phase in Sample 1 at

this temperature. The TTT diagrams at low temperatures confirmed that Sample 1, in which $Ca_5Al_6O_{14}$ was the main phase, exhibited a higher formation rate, and the precipitation of other dominant phases in Samples 2 to 4 did not significantly affect the incubation time at low temperature.

The precipitated phases at equilibrium were calculated using FactSage 7.1. The major crystalline phase was expected to be $Ca_{11}Si_4B_2O_{22}$, which, however, was not observed in the XRD analysis. Obviously, the equilibrium was not reached under the experimental conditions. Another possible reason was that the fluoride in mold fluxes suppressed the formation of $Ca_{11}Si_4B_2O_{22}$.

B. Crystallization and Heat Transfer

The decrease of crystallization tendency normally leads to a higher heat transfer rate due to the reduction of radiation at the grain boundary of crystals, the high thermal resistances of structural imperfections and air gaps.^[45–47] As indicated in CCT and TTT diagrams, the increase of B_2O_3 content decreased the crystallization tendency of mold fluxes. It is generally consistent with the variation of heat flux shown in Figure 14. The only discrepancy is that the increase of B_2O_3 content from 7.6 to 9.6 mass pct slightly suppressed the heat flux from 444 to 423 kW/m^2 in the heat transfer measurement. The reason is not confirmed, but it might be related to the incorporation of large borate structures into aluminate or silicate structures, which reduced the thermal conduction by disrupting phonon movement.^[20] Kim and Morita^[20] observed the decrease of thermal conductivity due to the incorporation of borate structures into silicate network with the increase of B_2O_3 content, even though the silicate network became more polymerized. In our experiments, this phenomenon should be more pronounced in the samples with lower amount of B_2O_3 where incorporation availability was sufficient. Therefore, it might lead to a lower heat transfer rate when B_2O_3 content increased from 7.6 to 9.6 mass pct as IET measured an overall heat transfer rate. However, such incorporation should play a less crucial role in the samples with higher concentrations of B_2O_3 where incorporation availability was limited. In this way, the effect of structure on thermal conduction was insignificant when B_2O_3 content increased from 9.6 to 13.1 mass pct as the major flux structures did not show visible change with the increase of B_2O_3 content in this range as demonstrated in Figure 13. The further increase of B_2O_3 content from 9.6 to 11.8 and 13.1 mass pct promoted the heat transfer as expected. Aside from the afore-mentioned reasons, the addition of B_2O_3 also reduced the liquidus temperature of mold fluxes. It decreased the thickness of crystalline layer and increased the ratio of liquid layer in the mold flux film in heat transfer measurement, which may also improve the heat flux.

V. CONCLUSIONS

The effect of B₂O₃ on crystallization, structure and heat transfer of CaO-Al₂O₃-based mold fluxes was investigated using SHTT/DHTT, Raman spectroscopy and IET, respectively. The major conclusions are summarized as follows:

- (1) CCT and TTT diagrams were constructed using SHTT. The crystallization tendency was inhibited with the increase of B₂O₃ content as shown in CCT diagram and the high-temperature region of TTT diagram. In the low-temperature region of TTT diagrams, the increase of B₂O₃ content from 7.6 to 9.6 mass pct increased the incubation time in the isothermal crystallization of mold fluxes but a further increase of B₂O₃ content to 13.1 pct did not show a significant change of incubation time. The crystallization process in a thermal field in DHTT experiments indicated that liquid, crystalline, and glassy layers were formed in the steady state;
- (2) XRD results showed that Ca₅Al₆O₁₄ was the dominant phase in Sample 1, especially at high temperatures. The increase of B₂O₃ concentration inhibited the formation of Ca₅Al₆O₁₄ and promoted the precipitation of Ca₃B₂O₆. The increase of B₂O₃ content also decreased the liquidus temperature of fluxes as no crystalline phase was observed in Sample 4 at 1373 K (1100 °C);
- (3) The increase of B₂O₃ content from 7.6 to 9.6 mass pct significantly increased the fraction of 3-D borate and aluminate units, e.g., [BO₄]-pentaborate and [AlO₄]⁵⁻ units and decreased the fraction of [SiO₄]⁴⁻ (Q⁰) units. A further increase of B₂O₃ concentration from 9.6 to 13.1 mass pct did not visibly affect the degree of polymerization based on fractions of major 3-D borate and aluminate structures, which was consistent with the insignificant change of crystallization behavior of mold fluxes in the low-temperature region when B₂O₃ content increased from 9.6 to 13.1 mass pct;
- (4) The increase of B₂O₃ content from 7.6 to 9.6 mass pct slightly decreased the heat flux from 444 ± 23.4 to 423 ± 17.2 kW/m². A further increase of B₂O₃ content to 11.8 and 13.1 mass pct increased the heat flux to 471 ± 19.6 and 517 ± 19.0 kW/m².

ACKNOWLEDGMENTS

Financial supports from Baosteel-Australia Joint Research and Development Centre (BAJC) and Australian Research Council (ARC) Industrial Transformation Hub (BA16006) are greatly acknowledged.

REFERENCES

1. D.R. Steinmetz, T. Jäpel, B. Wietbrock, P. Eisenlohr, I. Gutierrez-Urrutia, A. Saeed-Akbari, T. Hickel, F. Roters, and D. Raabe: *Acta Mater.*, 2013, vol. 61, pp. 494–510.

2. I. Gutierrez-Urrutia and D. Raabe: *Acta Mater.*, 2011, vol. 59, pp. 6449–62.
3. O. Grässel, L. Krüger, G. Frommeyer, and L.W. Meyer: *Int. J. Plast.*, 2000, vol. 16, pp. 1391–1409.
4. K. Sato, M. Ichinose, Y. Hirotsu, and Y. Inoue: *ISIJ Int.*, 1989, vol. 29, pp. 868–77.
5. D.T. Pierce, J.A. Jiménez, J. Bentley, D. Raabe, and J.E. Wittig: *Acta Mater.*, 2015, vol. 100, pp. 178–90.
6. A. Dumay, J.P. Chateau, S. Allain, S. Migot, and O. Bouaziz: *Mater. Sci. Eng. A*, 2008, vols. 483–484, pp. 184–87.
7. J.-W. Cho, K. Blazek, M. Frazee, H. Yin, J.H. Park, and S.-W. Moon: *ISIJ Int.*, 2013, vol. 53, pp. 62–70.
8. M.-S. Kim, S.-W. Lee, J.-W. Cho, M.-S. Park, H.-G. Lee, and Y.-B. Kang: *Metall. Mater. Trans. B*, 2013, vol. 44B, pp. 299–308.
9. Y.-B. Kang, M.-S. Kim, S.-W. Lee, J.-W. Cho, M.-S. Park, and H.-G. Lee: *Metall. Mater. Trans. B*, 2013, vol. 44B, pp. 309–16.
10. K. Blazek, H. Yin, G. Skoczylas, M. McClymonds, and M. Frazee: *Iron Steel Technol.*, 2011, vol. 8, p. 231.
11. Y. Sun, J. Liao, K. Zheng, X. Wang, and Z. Zhang: *JOM*, 2014, vol. 66, pp. 2168–75.
12. G.-R. Li, H.-M. Wang, Q.-X. Dai, Y.-T. Zhao, and J.-S. Li: *J. Iron Steel Res. Int.*, 2007, vol. 14, pp. 25–28.
13. A.B. Fox, K.C. Mills, D. Lever, C. Bezerra, C. Valadares, I. Unamuno, J.J. Laraudogoitia, and J. Gisby: *ISIJ Int.*, 2005, vol. 45, pp. 1051–58.
14. J.-Y. Park, G.H. Kim, J.B. Kim, S. Park, and I. Sohn: *Metall. Mater. Trans. B*, 2016, vol. 47B, pp. 2582–94.
15. B. Lu and W. Wang: *Metall. Mater. Trans. B*, 2015, vol. 46B, pp. 852–62.
16. B. Lu, K. Chen, W. Wang, and B. Jiang: *Metall. Mater. Trans. B*, 2014, vol. 45B, pp. 1496–1509.
17. H. Zhao, W. Wang, L. Zhou, B. Lu, and Y.-B. Kang: *Metall. Mater. Trans. B*, 2014, vol. 45B, pp. 1510–19.
18. Q. Liu, G. Wen, J. Li, X. Fu, P. Tang, and W. Li: *Ironmak. Steelmak.*, 2014, vol. 41, pp. 292–97.
19. J. Kline, M. Tangstad, and G. Tranell: *Metall. Mater. Trans. B*, 2015, vol. 46B, pp. 62–73.
20. Y. Kim and K. Morita: *ISIJ Int.*, 2014, vol. 54, pp. 2077–83.
21. J. Yang, J. Zhang, Y. Sasaki, O. Ostrovski, C. Zhang, D. Cai, and Y. Kashiwaya: *Metall. Mater. Trans. B*, 2017, vol. 48B, pp. 2077–91.
22. Z. Wang, Q. Shu, and K. Chou: *ISIJ Int.*, 2011, vol. 51, pp. 1021–27.
23. Y. Sun and Z. Zhang: *Metall. Mater. Trans. B*, 2015, vol. 46B, pp. 1549–54.
24. G.H. Kim and I. Sohn: *Metall. Mater. Trans. B*, 2014, vol. 45B, pp. 86–95.
25. D. Xiao, W. Wang, and B. Lu: *Metall. Mater. Trans. B*, 2015, vol. 46B, pp. 873–81.
26. L. Wang, Y. Cui, J. Yang, C. Zhang, D. Cai, J. Zhang, Y. Sasaki, and O. Ostrovski: *Steel Res. Int.*, 2015, vol. 86, pp. 670–77.
27. Y. Kashiwaya, C.E. Cicutti, and A.W. Cramb: *ISIJ Int.*, 1998, vol. 38, pp. 357–65.
28. Y. Kashiwaya, C.E. Cicutti, A.W. Cramb, and K. Ishii: *ISIJ Int.*, 1998, vol. 38, pp. 348–56.
29. J. Yang, Y. Cui, L. Wang, Y. Sasaki, J. Zhang, O. Ostrovski, and Y. Kashiwaya: *Steel Res. Int.*, 2015, vol. 86, pp. 636–43.
30. B. Ho: Master Thesis, University of Illinois at Urbana-Champaign, 1992.
31. K. Gu, W. Wang, L. Zhou, F. Ma, and D. Huang: *Metall. Mater. Trans. B*, 2012, vol. 43B, pp. 937–45.
32. L. Zhou, W. Wang, B. Lu, G. Wen, and J. Yang: *Met. Mater. Int.*, 2015, vol. 21, pp. 126–33.
33. J. Yang, J. Zhang, Y. Sasaki, O. Ostrovski, C. Zhang, D. Cai, and Y. Kashiwaya: *Metall. Mater. Trans. B*, 2016, vol. 47B, pp. 2447–58.
34. Y. Meng and B.G. Thomas: *ISIJ Int.*, 2006, vol. 46, pp. 660–69.
35. P. McMillan and B. Piriou: *J. Non-cryst. Solids*, 1983, vol. 55, pp. 221–42.
36. E. Gao, W. Wang, and L. Zhang: *J. Non-cryst. Solids*, 2017, vol. 473, pp. 79–86.
37. J. Gao, G. Wen, T. Huang, B. Bai, P. Tang, and Q. Liu: *J. Non-cryst. Solids*, 2016, vol. 452, pp. 119–24.
38. G.-H. Kim and I. Sohn: *J. Non-cryst. Solids*, 2012, vol. 358, pp. 1530–37.

39. J.H. Park, D.J. Min, and H.S. Song: *ISIJ Int.*, 2002, vol. 42, pp. 38–43.
40. P. Tarte: *Spectrochim. Acta A*, 1967, vol. 23, pp. 2127–43.
41. J. Qi, C. Liu, and M. Jiang: *J. Non-cryst. Solids*, 2017, vol. 475, pp. 101–07.
42. B. Cochain, D.R. Neuville, G.S. Henderson, C.A. McCammon, O. Pinet, P. Richet, and L. Pinckney: *J. Am. Ceram. Soc.*, 2012, vol. 95, pp. 962–71.
43. B.O. Mysen, D. Virgo, and C.M. Scarfe: *Am. Mineral.*, 1980, vol. 65, pp. 690–710.
44. L. Wang, C. Zhang, D. Cai, J. Zhang, Y. Sasaki, and O. Ostrovski: *Metall. Mater. Trans. B*, 2017, vol. 48B, pp. 516–26.
45. H. Nakada, M. Susa, Y. Seko, M. Hayashi, and K. Nagata: *ISIJ Int.*, 2008, vol. 48, pp. 446–53.
46. S. Ozawa, M. Susa, T. Goto, R. Endo, and K.C. Mills: *ISIJ Int.*, 2006, vol. 46, pp. 413–19.
47. J. Yang, J. Zhang, Y. Sasaki, O. Ostrovski, C. Zhang, D. Cai, and Y. Kashiwaya: *ISIJ Int.*, 2016, vol. 56, pp. 574–83.